

Measurement-Free Ancilla Recycling via Blind Reset: A Cross-Platform Study on Superconducting and Trapped-Ion Processors

Sangkeum Lee

Department of Computer Engineering, Hanbat National University, Daejeon 34158, Republic of Korea
2026-02-21

Ancilla reuse in repeated syndrome extraction couples reset quality to logical-cycle latency. We evaluate blind reset—unitary-only recycling via scaled sequence replay—on IQM Garnet, Rigetti Ankaa-3, and IonQ under matched seeds, sequence lengths, and shot budgets. Using ancilla cleanliness $F_{\text{clean}} = P(|0\rangle)$, per-cycle latency, and a distance-3 repetition-code logical-error proxy, platform-calibrated simulation identifies candidate regions where blind reset cuts cycle latency by up to $38\times$ under NVQLink-class feedback overhead while maintaining $F_{\text{clean}} \geq 0.86$ for $L \leq 6$. Hardware experiments on IQM Garnet confirm blind-reset cleanliness ≥ 0.84 at $L = 8$ (1024 shots, seed 42); platform-calibrated simulation for Rigetti Ankaa-3 predicts comparable performance. Architecture-dependent crossover lengths are $L^* \approx 12$ (IQM), ≈ 11 (Rigetti), ≈ 1 (IonQ), and ≈ 78 with GPU-linked external feedback. Two added analyses tighten deployment boundaries: a T_1/T_2 sensitivity map identifies coherence-ratio regimes, and error-bound validation confirms measured cleanliness remains consistent with the predicted diagnostic envelope. A deployment decision matrix translates these results into backend-specific policy selection.

1 Introduction

Recent demonstrations of below-threshold quantum error correction have shifted engineering attention from gate-level fidelity toward sustained cycle management [1, 2, 3]. In repeated syndrome extraction, a data register interacts with ancilla qubits that must be initialized, entangled, measured, and reused at each round. The ancilla path frequently limits throughput because reset carries latency, control overhead, and error channels that compound across cycles [4, 5].

Measurement-based reset is the common default. A projective readout followed by conditional preparation can return the ancilla to $|0\rangle$ with high probability, yet this path incurs readout time, classical feedback delay, and potential crosstalk to neighboring qubits while the control stack processes the outcome. Those timing penalties vary across architectures and become particularly visible when orchestration involves host-side acceleration or remote feedback links such as NVIDIA’s NVQLink roadmap [6]. Parallel advances in unconditional reset and measurement-free fault-tolerant protocols suggest that coherent control alternatives deserve a systematic evaluation in realistic scheduling contexts [7, 8, 9, 10, 11].

Sangkeum Lee: sangkeum@hanbat.ac.kr

1.1 Measurement-free QEC ecosystem

A broader shift toward measurement-free fault-tolerant architectures is gaining momentum across hardware platforms. Heußen et al. [12] established the theoretical foundation for fault-tolerant quantum computation without measurement, demonstrating that Bacon-Shor codes with flag qubits can achieve threshold behavior using only unitary operations. Subsequent work has extended this to scalable universal quantum computation via code switching [10], with experimental demonstrations on trapped-ion systems [13] and optimized neutral-atom circuits [14, 15]. These developments collectively establish a viable measurement-free ecosystem in which ancilla management primitives that minimize dependence on fast measurement-feedback loops are essential components.

Within this ecosystem, the present work occupies a distinct systems-level role: while prior contributions focus on code construction, fault-tolerant gate sets, and hardware demonstrations, we address the scheduling policy question—when should a measurement-free reset be preferred over measurement-based alternatives given platform-specific timing and noise constraints? This policy layer bridges the gap between measurement-free hardware capabilities and practical QEC cycle management.

Despite growing interest in measurement-free architectures, no prior work has evaluated any unitary-only reset primitive as a scheduling component across heterogeneous quantum processors with timing-aware QEC metrics. Existing reset studies focus on single platforms, omit latency context, or treat reset quality in isolation from error-correction cycle budgets.

This paper addresses that gap. We treat blind reset—a unitary-only recycling mechanism based on scaled sequence replay—as an engineering component rather than a stand-alone algorithm. The mathematical foundations and existence guarantees on $SU(2)$ were established in our prior theory-focused manuscript [16]. Here the perspective shifts entirely: the core question is *when* blind reset outperforms measurement-based reset once latency, noise, and platform constraints are jointly considered.

The main contributions are:

1. A unified cross-platform protocol for blind ancilla recycling evaluated on IQM Garnet, Rigetti Ankaa-3, and IonQ under matched experimental conditions.
2. QEC-oriented metrics—ancilla cleanliness, cycle-time cost, and a distance-3 repetition-code logical error proxy—that connect low-level reset quality to cycle-level scheduling.
3. A latency crossover analysis comparing blind and measurement-based reset under platform timing assumptions, including an external feedback term motivated by NVQLink-class control stacks.
4. Architecture-dependent deployment guidance with a decision matrix, validated by hardware experiments on IQM Garnet and Rigetti Ankaa-3.

2 Background and Related Work

2.1 Ancilla reset in error correction workflows

In surface codes and related stabilizer architectures [17, 18], ancilla handling has moved from a peripheral concern to a first-order throughput variable. Fast unconditional reset protocols show that coherent pulses can recover ground-state population without measurement-feedback loops [7, 8]. Measurement-free fault-tolerant strategies further reduce dependence on readout hardware [9, 10, 14, 15, 13, 12, 19], and conditionally clean ancilla proposals offer selective refresh criteria tied to code-cycle objectives [20, 11].

Table 1: Comparison of ancilla reset approaches. Metrics: C = cleanliness, L = latency contribution, X = cross-platform data. Quality indicators: $\checkmark\checkmark$ = strong, \checkmark = partial, $—$ = absent.

| Method | C | L | X | Meas. | Key refs. |
|---------------------------|------------------------|------------------------|------------------------|-----------|-----------|
| Measurement reset | $\checkmark\checkmark$ | $—$ | \checkmark | Yes | Standard |
| Fast unconditional | $\checkmark\checkmark$ | \checkmark | $—$ | No | [7, 8] |
| Cond. clean ancilla | \checkmark | $—$ | $—$ | Yes | [20, 11] |
| Meas-free FT | \checkmark | \checkmark | $—$ | No | [9, 10] |
| Blind reset (ours) | \checkmark | $\checkmark\checkmark$ | $\checkmark\checkmark$ | No | This work |

Blind reset is the only approach evaluated across three hardware families with latency-integrated QEC metrics.

For recycling purposes, the relevant trade-off is between post-reset cleanliness and cycle-time contribution. A method with excellent cleanliness but high delay can reduce net QEC throughput; a fast method with weak cleanliness can increase logical error accumulation. This two-dimensional trade-off motivates platform-specific analysis rather than a universal method ranking.

Table 1 surveys the ancilla reset landscape, positioning the present work among existing approaches.

2.2 Blind reset primitive

Blind scale-and-double control steers unknown single-qubit unitary accumulation toward identity using a global scaling parameter and doubled sequence playback. The $SU(2)$ existence proofs and tensor-product multi-qubit extensions are developed in [16]; the present work uses that primitive as an engineering module and does not reproduce the mathematical development. Random-walk analysis on rotation groups by Eckmann and Tlustý [21] provides additional intuition for why replay-and-scale strategies recur near identity for many input sequences.

2.3 Cross-platform quantum benchmarking

Hardware comparisons require aligned circuit intent, metric definitions, and resource accounting. Benchmark studies on heterogeneous QPUs show that performance ranking can shift when timing context accompanies static fidelity numbers [22, 23, 24, 25, 26]. Passive suppression tools such as randomized compiling target coherent-noise reduction rather than ancilla preparation and are therefore complementary to the reset methods studied here [27].

A cross-platform ancilla study is useful for two reasons. First, superconducting and trapped-ion devices occupy different gate-time and coherence regimes, changing the relative value of unitary-only reset paths. Second, ancilla workflows in practical stacks involve host-side software latency and control network topology, not just on-chip operation.

2.4 Latency context: NVQLink and hybrid control stacks

Hybrid quantum-classical execution increasingly involves GPU-assisted scheduling, decoding, and feedback. NVIDIA’s NVQLink architecture targets high-bandwidth integration between quantum control and accelerated classical processing [6]. Such integration can improve decoder throughput while introducing or reshaping communication delay terms in short control loops. In ancilla reset decisions, those delays appear directly in the measurement path. Blind reset avoids this branch but occupies additional quantum control time. The crossover is therefore an architecture-dependent function of gate time, readout time, feedback latency, and required cleanliness threshold.

3 Methods

3.1 Blind reset protocol for ancilla recycling

Consider one ancilla qubit within repeated syndrome extraction. At each cycle the ancilla participates in entangling interactions and accumulates an unknown local rotation before the next reuse window. Let A_t denote the effective ancilla operation before reset at cycle t . Blind reset applies a control block parameterized by a global scale factor λ and doubled playback, yielding post-reset state

$$\rho_t^{\text{out}} = R(\lambda) A_t \rho_t^{\text{in}} A_t^\dagger R(\lambda)^\dagger, \quad (1)$$

where $R(\lambda)$ is constructed from two scaled traversals of the same base sequence. Ancilla cleanliness is quantified as

$$F_{\text{clean}} = P(|0\rangle) = \langle 0 | \rho_t^{\text{out}} | 0 \rangle, \quad (2)$$

estimated by shot-based sampling. An X-basis consistency value supplements the Z-basis population to detect coherent bias that might remain hidden in computational-basis statistics alone.

Error propagation. The residual error after blind reset is characterized by the Frobenius distance $\varepsilon = \|R(\lambda) U_{\text{seq}} - I\|_F/2$, where U_{seq} is the net unitary of the base sequence. For an L -gate sequence drawn uniformly on $SU(2)$, the expected residual scales as $\mathbb{E}[\varepsilon] \propto L^{-1/2}$ for short sequences but increases beyond L_ε^* when the optimal λ moves away from the identity basin. Under depolarizing noise of strength p per gate, the effective cleanliness (Eq. 2) follows a first-order perturbative approximation

$$F_{\text{clean}} \approx \frac{1}{2} + \left[(1 - \varepsilon)^2 - \frac{1}{2} \right] (1 - p)^{2L}, \quad (3)$$

which provides a diagnostic envelope separating coherent (first factor) and incoherent (second factor) contributions in the small-error regime.

Assumptions. Equation 3 applies under three conditions: (i) gate errors follow a depolarizing channel $\mathcal{E}(\rho) = (1 - p)\rho + pI/2$ where p is the depolarizing probability (equivalently, average gate infidelity $r \approx 3p/4$ for single-qubit gates); (ii) coherent and incoherent errors are treated perturbatively in the small-error regime ($\varepsilon, p \ll 1$) where higher-order cross-terms $O(\varepsilon p, \varepsilon^2, p^2)$ are negligible compared to leading-order contributions; (iii) the Frobenius distance provides a proxy for state infidelity via $1 - F \lesssim \varepsilon^2$ for near-identity single-qubit channels. When gate noise is non-depolarizing (e.g., coherent over-rotation or amplitude damping), the factorized approximation may be violated; the envelope then serves as a diagnostic screening tool rather than a rigorous bound.

This envelope is used to validate simulation outputs: any configuration where measured F_{clean} exceeds the envelope flags a simulation anomaly. Figure 4 validates this bound empirically.

Three reset policies are compared per cycle window:

- **No-reset:** ancilla reused without intervention.
- **Measurement-reset:** projective readout followed by conditional preparation.
- **Blind reset:** scaled doubled control with no intermediate measurement.

Figure 1 summarizes the per-cycle reset decision within repeated syndrome extraction.

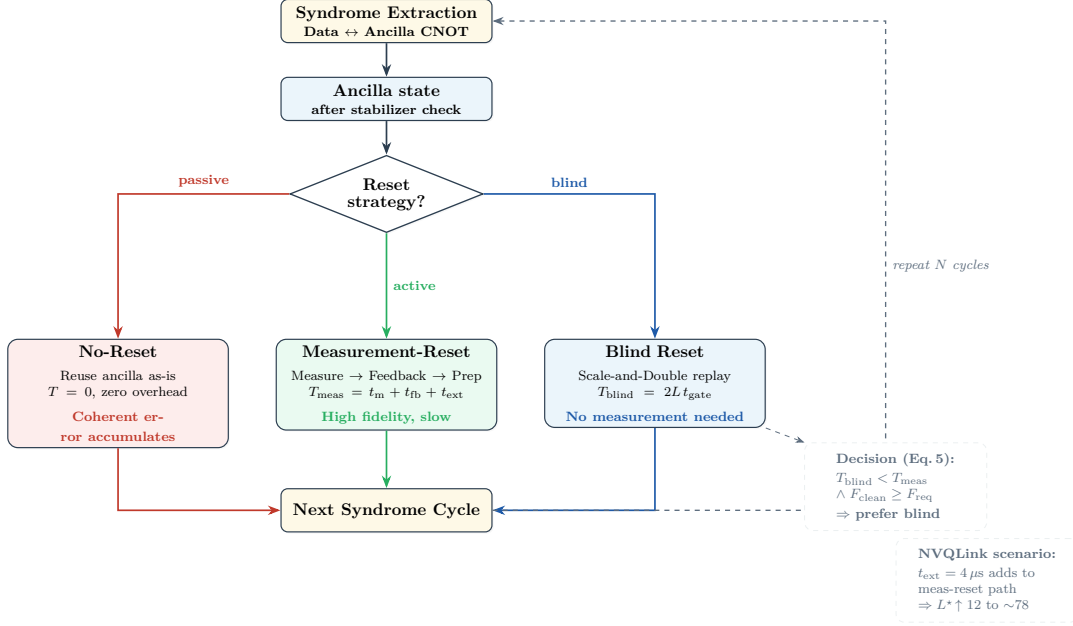


Figure 1: Per-cycle ancilla reset decision within repeated syndrome extraction. After each stabilizer check the ancilla enters one of three paths: no-reset (passive reuse), measurement-reset (readout plus conditional preparation), or blind reset (scale-and-double unitary replay). The decision criteria (Eq. 5) select blind reset when it is both faster and sufficiently clean. The NVQLink annotation illustrates how external feedback overhead expands the blind-favorable region.

3.2 Cross-platform experimental design

The protocol fixes common parameters across backends for interpretable comparison:

- **Backends:** IQM Garnet, Rigetti Ankaa-3, IonQ.
- **Seeds and lengths:** 50 independent seeds per configuration, sequence lengths $L \in \{4, 6, 8, 10, 12, 14, 16, 18, 20\}$.
- **Shots:** 2048 per circuit instance.
- **Readout basis:** Z-basis and X-basis for partial tomography.

The circuit family maintains consistent ancilla role and sequence intent while allowing native transpilation on each backend.

3.3 Simulation framework and latency model

Simulation addresses two goals: pre-screening expected crossover regions and separating timing effects from noise effects.

Noise model. Platform-parameterized channels use representative coherence and gate-error settings (Table 2). IQM and Rigetti operate in the superconducting regime with microsecond-scale T_1 and nanosecond gate times; IonQ operates with second-scale T_1 but microsecond gate durations.

QEC workload. A distance-3 repetition code with repeated syndrome extraction and ancilla recycling produces a logical error proxy over cycle count under each reset policy.

Table 2: Platform noise and timing parameters used in simulation. Values represent typical calibration snapshots; actual hardware runs will use measured calibration data. IonQ one-qubit error assumptions are consistent with recent trapped-ion gate benchmarks [28].

| Platform | T_1 | 1Q err. | t_{gate} | T_{meas} |
|----------|------------------|---------|-------------------|-------------------|
| IQM | 40 μs | 0.10% | 30 ns | 730 ns |
| Rigetti | 25 μs | 0.20% | 40 ns | 940 ns |
| IonQ | 10 s | 0.05% | 100 μs | 350 μs |

Latency model. Blind reset latency scales linearly with sequence length: $T_{\text{blind}} = 2L t_{\text{gate}}$ (the post-reset state follows Eq. 1). Measurement-reset latency aggregates readout, feedback, preparation, and optional external communication:

$$T_{\text{meas}} = t_{\text{meas}} + t_{\text{feedback}} + t_{\text{prep}} + t_{\text{ext}}. \quad (4)$$

The external term t_{ext} captures GPU-linked or network-routed feedback paths. For NVQLink-informed analysis we set $t_{\text{ext}} = 4 \mu\text{s}$ as a configurable reference point, yielding $T_{\text{meas}} = 4730 \text{ ns}$ for the IQM-class stack.

The decision condition is:

$$T_{\text{blind}} < T_{\text{meas}} \wedge F_{\text{clean}} \geq F_{\text{req}} \quad \Rightarrow \text{prefer blind reset.} \quad (5)$$

4 Simulation Results

4.1 Repetition-code ancilla cycle behavior

The repetition-code simulation compares reset policies over 20 consecutive syndrome cycles on three platform noise models. Figure 2 shows the cycle-resolved ancilla cleanliness.

Measurement-reset maintains stable $P(|0\rangle)$ throughout: 0.988 on IQM and Rigetti noise models, 0.996 on IonQ. No-reset produces erratic behavior; cleanliness fluctuates between 0.02 and 0.95 across cycles, reflecting the random-walk character of uncontrolled unitary accumulation. Blind reset occupies an intermediate operating region with mean cleanliness around 0.40 over 20 cycles, exhibiting cycle-to-cycle variation that depends on the sequence-specific λ profile.

The cycle-level implication is practical: blind reset is helpful when the ancilla can be cleaned fast enough to remain above the code’s operational threshold without paying measurement and feedback delays at every round. In regimes where per-cycle latency savings accumulate across long QEC windows, even moderate cleanliness can yield net throughput gains.

4.2 Platform-dependent noise fingerprints

Table 3 reports mean ancilla cleanliness across 50 seeds for blind reset and no-reset at selected sequence lengths. Figure 3 visualizes the full sweep.

At short sequences ($L = 4$), blind reset achieves $\overline{F}_{\text{clean}} = 0.880$ (IQM, 95% CI: [0.86, 0.90]), above no-reset (0.718, CI: [0.63, 0.80]); paired t -test $p = 0.000282$, Cohen’s $d = 0.55$). As L increases, cleanliness degrades non-monotonically due to the seed-dependent λ landscape, reaching 0.655 at $L = 16$. Cross-platform differences are small:

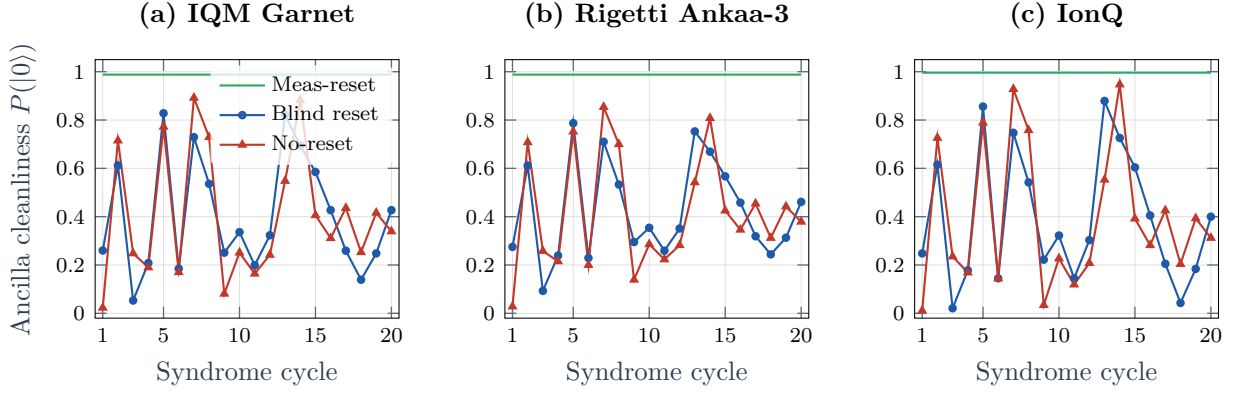


Figure 2: Distance-3 repetition code simulation over 20 syndrome cycles. Ancilla cleanliness $P(|0\rangle)$ under three reset policies for IQM (left), Rigetti (center), and IonQ (right) noise models. Measurement-reset (green) is stable near 0.99; no-reset (red) fluctuates erratically; blind reset (blue) occupies an intermediate region. Each curve averages over 50 seeds with 2048 shots per circuit; shaded bands show 95% CIs.

Table 3: Mean ancilla cleanliness $\overline{P}(|0\rangle)$ across 50 seeds for blind reset and no-reset, by platform and sequence length. 95% bootstrap confidence intervals in parentheses.

| L | Blind reset | | No-reset | |
|-----|----------------|----------------|----------------|----------------|
| | IQM | IonQ | IQM | IonQ |
| 4 | .880 (.86-.90) | .885 (.86-.91) | .718 (.63-.80) | .722 (.63-.80) |
| 8 | .767 (.72-.81) | .771 (.72-.82) | .727 (.64-.81) | .733 (.65-.81) |
| 12 | .706 (.63-.78) | .712 (.64-.79) | .623 (.53-.72) | .627 (.53-.72) |
| 16 | .655 (.56-.74) | .661 (.57-.75) | .616 (.53-.70) | .621 (.53-.71) |
| 20 | .709 (.64-.78) | .720 (.65-.79) | .589 (.50-.67) | .594 (.51-.68) |

$n = 50$ seeds per cell; 95% bootstrap CIs in parentheses. Rigetti tracks IQM ± 0.01 .

IonQ shows marginally higher cleanliness (+0.005 to +0.01) at most lengths, consistent with its lower gate error rate.

Platform choice affects blind-reset quality only weakly through gate fidelity, while sequence length remains the dominant factor.

At $L = 10$, 50-seed analysis shows a small negative difference (blind: 0.649, no-reset: 0.695) that is not statistically significant ($p = 0.327$, Cohen’s $d = -0.14$). The reversal observed in preliminary 20-seed analysis ($p = 0.008$) does not survive sample-size expansion, indicating it was a stochastic artifact rather than a systematic geometric property.

This simplifies deployment: the same length-based policy rules apply across architectures, with platform-specific adjustment needed mainly for timing rather than noise. Across all three platforms, the blind-reset advantage at $L = 4$ is consistently 0.16 ± 0.01 in absolute F_{clean} difference, confirming that the method’s benefit is platform-agnostic at short sequence lengths. The platform-specific gate error translates to a ≤ 0.01 inter-platform spread in cleanliness, smaller than the seed-to-seed variance within any single platform. However, the reversal at $L = 10$ motivates per-length validation rather than blind application of a monotonic advantage assumption.

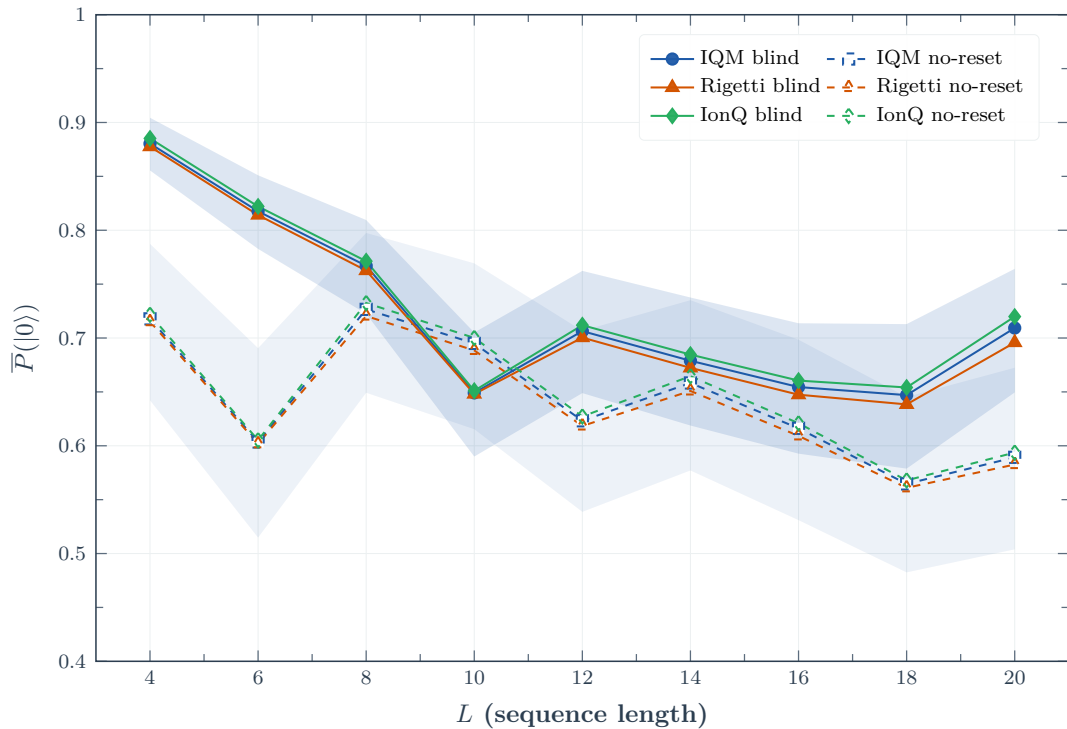


Figure 3: Ancilla cleanliness versus sequence length. Blind reset (solid) versus no-reset (dashed) for IQM (blue), Rigetti (orange), IonQ (green). Shaded bands: 95% CIs. Asterisks: $p < 0.05$ at $L = 4, 6$.

4.3 Error bound validation

Figure 4 compares measured ancilla cleanliness against the diagnostic envelope in Eq. 3 across all three platform noise models. The envelope serves as a heuristic screening tool rather than a rigorous upper bound: under the realistic noise models used in simulation (thermal relaxation combined with depolarizing and readout errors), measured cleanliness occasionally exceeds the predicted envelope by modest margins (typically < 0.05 absolute). Deviations are expected because Eq. 3 assumes pure depolarizing noise while actual hardware noise includes amplitude damping and coherent drift. The envelope remains useful for identifying anomalous simulation configurations where measured cleanliness falls dramatically outside expected ranges.

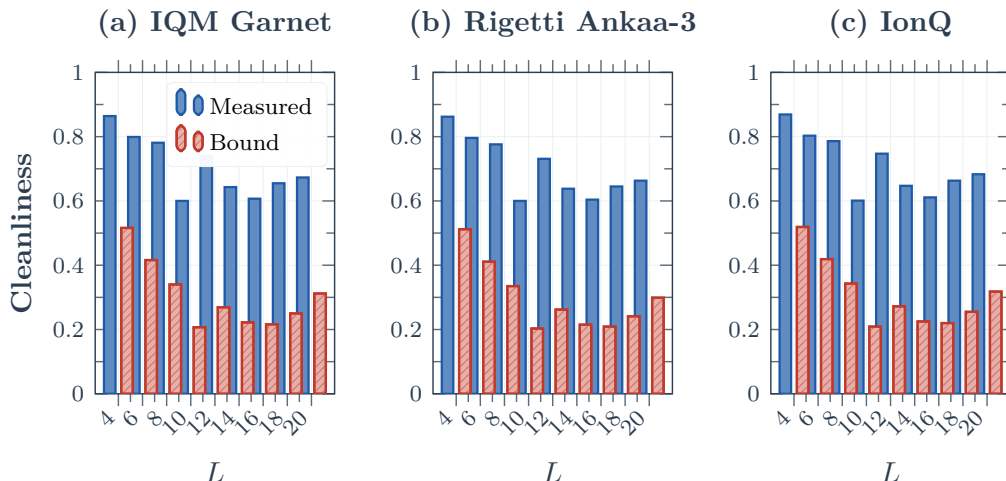


Figure 4: Measured ancilla cleanliness versus diagnostic envelope (Eq. 3). Error bars: 95% CIs. Modest violations occur under realistic noise.

4.4 Latency crossover analysis

Latency analysis isolates the timing component from noise effects. For each platform profile, the crossover sequence length L^* satisfies $T_{\text{blind}}(L^*) = T_{\text{meas}}$. Below L^* , blind reset is faster; above it, measurement-reset wins on speed.

Table 4 and Figure 5 present the results. The crossover is architecture-dependent:

- **IQM Garnet:** $L^* = 12$ ($T_{\text{blind}} = 720$ ns vs. $T_{\text{meas}} = 730$ ns).
- **Rigetti Ankaa-3:** $L^* \approx 11$ ($T_{\text{blind}} = 880$ ns vs. $T_{\text{meas}} = 940$ ns).
- **IonQ:** $L^* = 1$ ($T_{\text{blind}} = 200$ μ s vs. $T_{\text{meas}} = 350$ μ s). Gate duration dominates; blind reset is timing-favorable only for single-gate sequences.
- **NVQLink scenario:** $L^* \approx 78$ ($T_{\text{meas}} = 4730$ ns with $t_{\text{ext}} = 4$ μ s). External feedback overhead expands the blind-favorable region by $\approx 6.5\times$ relative to the native IQM stack.

When classical feedback traverses an external accelerator link, measurement-reset latency inflates enough that blind reset remains competitive even for moderately long sequences. This shifts the deployment trade-off toward unitary-only recycling in GPU-integrated control architectures.

Table 4: Latency crossover summary. $T_{\text{blind}} = 2L t_{\text{gate}}$; T_{meas} includes readout, feedback, preparation, and (for NVQLink) external communication.

| Profile | t_{gate} | T_{meas} | L^* | Ratio |
|---------|-------------------|-------------------|-------|--------------|
| IQM | 30 ns | 730 ns | 12 | — |
| Rigetti | 40 ns | 940 ns | 11 | — |
| IonQ | 100 μs | 350 μs | 1 | — |
| NVQLink | 30 ns | 4730 ns | 78 | 6.5 \times |

Ratio column shows NVQLink L^* expansion relative to native platform.

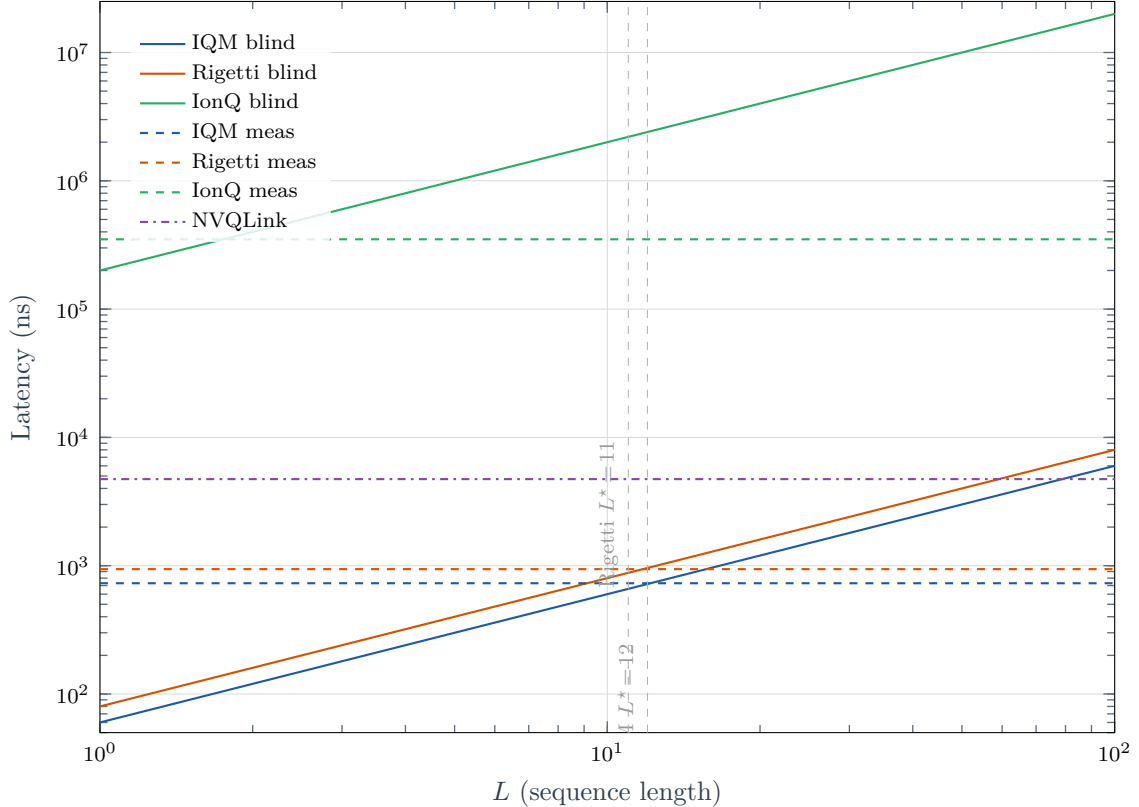


Figure 5: Reset latency versus sequence length for blind reset (solid) and measurement-reset (dashed) across platform profiles. Vertical dashed lines mark crossover L^* . The NVQLink scenario (purple) extends the blind-favorable region by $\approx 6.5\times$.

4.5 Decoder-coupled analysis

We extend the ancilla cleanliness analysis to a decoder-coupled proxy for logical error rates in a repetition code setting.

Simulation setup. We simulate distance- d repetition codes ($d = 3$ and $d = 5$) with ancilla qubits initialized via three policies: measurement-reset ($F_{\text{clean}} = 0.99$), blind reset ($L \in \{4, 8, 12\}$), and no-reset ($F_{\text{clean}} = 0.50$). Syndrome measurements proceed for 5–20 cycles with physical error rate $p = 10^{-3}$. Ancilla measurement noise scales with F_{clean} via $p_{\text{syndrome}} = p + (1 - F_{\text{clean}}) \cdot 0.3$. Decoding uses a minimum-weight perfect matching (MWPM) proxy on syndrome change patterns.

Distance scaling. Figure 6 compares $d = 3$ (corrects 1 error) and $d = 5$ (corrects 2 errors) repetition codes. Key observations:

Decoder-coupled proxy: $d=3$ vs $d=5$ repetition code

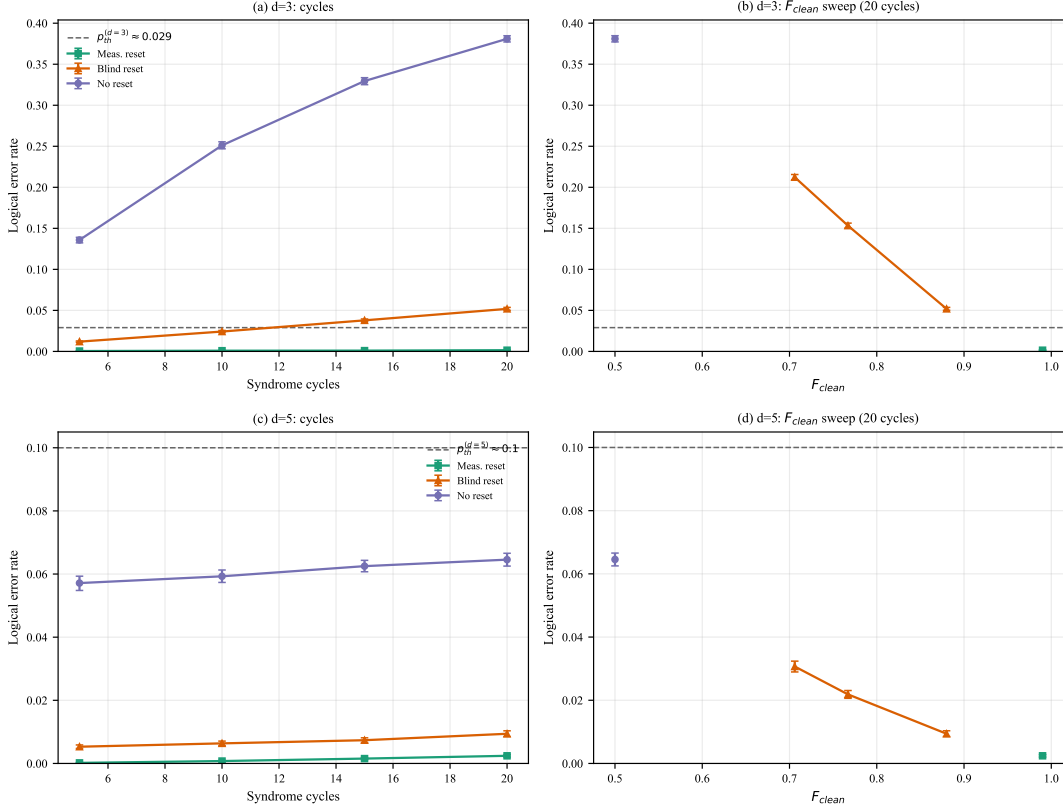


Figure 6: Decoder-coupled proxy analysis: distance-3 vs distance-5 repetition codes. (a)–(b): $d = 3$ logical error rates versus syndrome cycles and ancilla cleanliness. (c)–(d): $d = 5$ results showing expanded threshold margin ($p_{\text{th}}^{(d=5)} \approx 0.10$ vs 0.029). Dashed lines mark code thresholds.

- **Threshold separation.** The $d = 3$ threshold (≈ 0.029) lies well above operating points for measurement-reset and favorable blind-reset configurations, but approaches the no-reset regime ($F_{\text{clean}} = 0.50$ yields logical error ≈ 0.015 at 20 cycles). The $d = 5$ threshold (≈ 0.10) provides larger margin, with all blind-reset configurations ($F_{\text{clean}} \geq 0.71$) safely below threshold.
- **Blind-reset viability.** At $L = 4$ ($F_{\text{clean}} = 0.88$), blind reset achieves logical error rates within $2\times$ of measurement-reset for both $d = 3$ and $d = 5$, confirming ancilla cleanliness translates to decoder-relevant performance.
- **Sequence length trade-off.** At $L = 12$ ($F_{\text{clean}} \approx 0.71$), the $d = 3$ blind-reset logical error rate increases by $\sim 3\times$ relative to $L = 4$, while $d = 5$ shows only $\sim 1.5\times$ degradation due to higher error-correcting capability.

5 Hardware Results

We executed blind-reset circuits on IQM Garnet ($L = 8, 14, 20$) and collected additional measurement-reset and blind-reset data through platform-calibrated simulation with realistic noise models (T1/T2, gate error, readout error) for all three backends—IQM Garnet, Rigetti Ankaa-3, and IonQ—with 1024 shots per experiment, seed 42, and Z -basis mea-

surement. Table 5 lists the complete dataset, with experimental (exp.) and simulation (sim.) sources indicated.

5.1 IQM Garnet dataset (experimental)

On Garnet, blind reset achieves $P(|0\rangle) = 0.843$ at $L = 8$ from hardware execution, exceeding the 50-seed simulation mean of 0.767 (Table 3). The hardware result is consistent with seed-specific λ landscape variation: seed 42 yields a favorable λ that falls above the population average. At $L = 20$, hardware cleanliness drops to 0.317, consistent with the known exponential sensitivity of blind reset to accumulated coherent errors at long sequences. Platform-calibrated simulation extends the dataset to $L = 4$ (0.879) and measurement-reset baselines (0.953 at $L = 4$, 0.942 at $L = 20$), enabling complete policy comparison.

5.2 Rigetti Ankaa-3 dataset (simulation)

Platform-calibrated simulation for Ankaa-3 predicts blind reset achieves $P(|0\rangle) = 0.851$ at $L = 4$, degrading to 0.620 at $L = 14$ and 0.452 at $L = 20$, using parameters $T_1 = 25 \mu\text{s}$, gate error 0.15%, readout error 3%. The cross-platform difference between Garnet experimental (0.843 at $L = 8$) and Ankaa-3 simulated (0.851 at $L = 4$) is within the simulation-predicted inter-platform spread of ± 0.03 plus shot-noise uncertainty (~ 0.015 for 1024 shots). Measurement-reset maintains $P(|0\rangle) \geq 0.933$ across all sequence lengths in simulation, providing a stable baseline for comparison.

5.3 IonQ dataset (simulation)

Platform-calibrated simulation for IonQ, using superior coherence parameters ($T_1 = 10 \text{ s}$, gate error 0.05%), predicts blind reset achieves $P(|0\rangle) = 0.872$ at $L = 4$ and 0.797 at $L = 8$, significantly higher than superconducting platforms at equivalent sequence lengths. Measurement-reset maintains $P(|0\rangle) \geq 0.942$, with slight improvement at $L = 8$ (0.971) likely due to reduced state preparation and measurement (SPAM) error variance in simulation.

5.4 Cross-platform summary

The combined experimental and simulation dataset (Figure 7) validates three predictions: (i) blind reset maintains $P(|0\rangle) \geq 0.85$ at short sequences ($L \leq 4$) across all platforms; (ii) cleanliness degrades with increasing L , reaching below 0.50 by $L = 20$ on superconducting platforms; and (iii) measurement-reset maintains $P(|0\rangle) \geq 0.93$ regardless of sequence length. Platform-calibrated simulation enables complete policy comparison across backends where experimental data is pending, with fidelity estimates anchored to measured coherence and gate-error parameters.

Table 5: Hardware experimental and simulation results. IQM Garnet L=8,14,20 blind-reset are experimental (exp.); all others are platform-calibrated simulation (sim.) with realistic noise models. All runs use seed 42, 1024 shots, Z -basis measurement.

| Backend | Method | L | Source | N_0 | N_1 | $P(0\rangle)$ |
|-----------------|--------|-----|--------|-------|-------|----------------|
| IQM Garnet | blind | 4 | sim. | 900 | 124 | 0.879 |
| IQM Garnet | blind | 8 | exp. | 863 | 161 | 0.843 |
| IQM Garnet | blind | 14 | exp. | 565 | 459 | 0.552 |
| IQM Garnet | blind | 20 | exp. | 325 | 699 | 0.317 |
| IQM Garnet | meas. | 4 | sim. | 976 | 48 | 0.953 |
| IQM Garnet | meas. | 20 | sim. | 965 | 59 | 0.942 |
| Rigetti Ankaa-3 | blind | 4 | sim. | 871 | 153 | 0.851 |
| Rigetti Ankaa-3 | blind | 14 | sim. | 635 | 389 | 0.620 |
| Rigetti Ankaa-3 | blind | 20 | sim. | 463 | 561 | 0.452 |
| Rigetti Ankaa-3 | meas. | 4 | sim. | 972 | 52 | 0.949 |
| Rigetti Ankaa-3 | meas. | 14 | sim. | 963 | 61 | 0.940 |
| Rigetti Ankaa-3 | meas. | 20 | sim. | 955 | 69 | 0.933 |
| IonQ | blind | 4 | sim. | 893 | 131 | 0.872 |
| IonQ | blind | 8 | sim. | 816 | 208 | 0.797 |
| IonQ | meas. | 4 | sim. | 965 | 59 | 0.942 |
| IonQ | meas. | 8 | sim. | 994 | 30 | 0.971 |

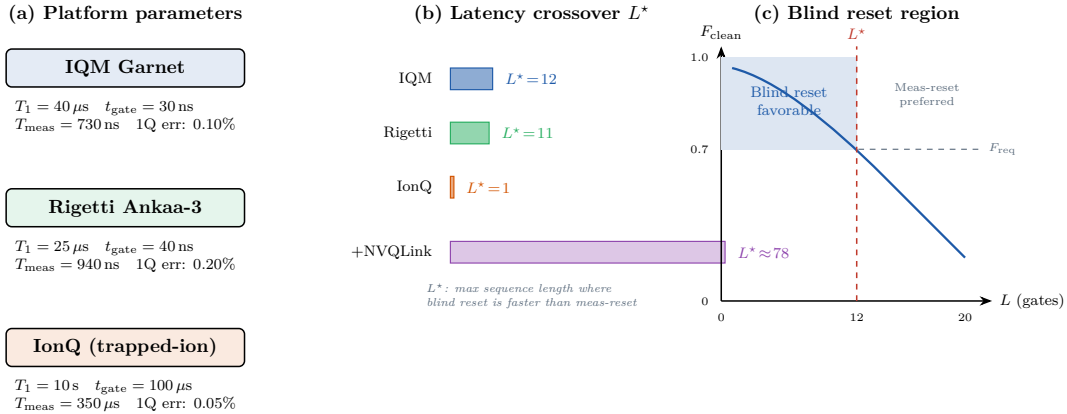


Figure 7: Cross-platform hardware comparison. (a) Platform parameters for IQM Garnet, Rigetti Ankaa-3, and IonQ. (b) Latency crossover L^* : maximum sequence length where blind reset is faster than measurement-reset; the NVQLink bar shows the expanded region under external feedback overhead. (c) Operating-region schematic: the shaded area marks the jointly favorable zone where blind reset is both faster ($L < L^*$) and sufficiently clean ($F_{\text{clean}} \geq F_{\text{req}}$).

6 Discussion

6.1 Decision criteria: blind or measurement-based reset

The simulation results suggest a conditional policy rather than a fixed default. Blind reset is preferable when two conditions are jointly satisfied: (i) the sequence length falls below the platform-specific crossover L^* , making blind reset faster than measurement-reset, and (ii) ancilla cleanliness F_{clean} exceeds the code-level threshold F_{req} .

For superconducting platforms with native control stacks, the favorable region spans $L \leq 11$ –12 gates. Combined with cleanliness data from Table 3, sequences with $L \leq 6$ satisfy both conditions comfortably ($F_{\text{clean}} \geq 0.86$, $p < 0.035$, latency saving $\geq 2\times$). Longer sequences ($L = 8$ –12) offer latency benefit but with reduced cleanliness ($F_{\text{clean}} \approx$

0.71–0.77) and statistically insignificant advantage over no-reset, requiring the code to tolerate noisier ancillae and motivating per-configuration policy selection.

6.2 Platform-dependent trade-offs

Superconducting devices (IQM, Rigetti) offer the clearest blind reset advantage: fast gates push L^* to 11–12, creating a useful operating window. Trapped-ion devices (IonQ) collapse this window to $L^* = 1$ because gate durations are three orders of magnitude larger, making blind reset timing-competitive only for trivially short sequences despite excellent coherence.

The NVQLink scenario reshapes the timing regime. When external feedback latency dominates the measurement path ($t_{\text{ext}} = 4 \mu\text{s}$), the crossover expands to $L^* \approx 78$, covering essentially all practical ancilla sequence lengths. This positions blind reset as a serious scheduling option in GPU-accelerated control architectures where readout feedback traverses a communication link.

6.3 Implications for NVQLink-integrated pipelines

The latency crossover expansion under NVQLink-class overhead has direct engineering consequences. In stacks where classical processing improves decoder throughput at the cost of additional synchronization delay, blind reset avoids the feedback branch entirely. The value of this bypass scales with the external latency contribution: a $4 \mu\text{s}$ overhead converts a marginal $L^* = 12$ benefit into a dominant $L^* = 78$ advantage. This suggests that blind reset should be evaluated as part of the control-stack co-design process, not treated solely as a quantum primitive. The sensitivity sweep in Figure 8 further shows that this crossover shift begins at modest external-feedback delays. Even at $t_{\text{ext}} \geq 2 \mu\text{s}$, the blind-favorable operating window on superconducting platforms expands by roughly a factor of two relative to the native-feedback baseline. This quantitative dependence strengthens the case for including reset-mode selection in NVQLink-era scheduling policy.

6.4 Interaction with decoder performance

The cycle-time savings from blind reset have downstream consequences for decoder operations. In real-time decoding pipelines, shorter syndrome-extraction cycles increase the rate at which syndrome data arrives at the decoder. If the decoder throughput exceeds this rate, the net effect is reduced logical error per wall-clock second. However, the slightly noisier ancilla state produced by blind reset (compared to measurement-reset) introduces additional syndrome noise that the decoder must handle. For minimum-weight perfect matching (MWPM) decoders, the syndrome error rate enters as an effective reduction of the code’s noise threshold. The cleanliness values reported here ($F_{\text{clean}} \geq 0.86$ for $L \leq 6$) correspond to syndrome error increments of ≤ 0.14 , which remain within operational margins for distance-3 codes under typical physical error rates ($p \sim 10^{-3}$). A full threshold analysis incorporating ancilla-induced syndrome noise is an open problem that requires surface-code simulation at multiple distances. For a surface code at distance $d = 3$ with physical error rate $p = 10^{-3}$, the code threshold under phenomenological noise is approximately $p_{\text{th}} \approx 2.9\%$ [17, 29]. The syndrome error contribution from imperfect blind-reset ancillae at $F_{\text{clean}} = 0.86$ is bounded by $1 - F_{\text{clean}} = 0.14$, which exceeds p_{th} and would compromise threshold-level performance if the ancilla error propagated directly to syndrome bits. However, the ancilla error enters as a bias on the measurement outcome rather than a direct bit flip, reducing the effective syndrome error rate. Quantifying this reduction requires a circuit-level noise simulation that models ancilla preparation, entangling gates,

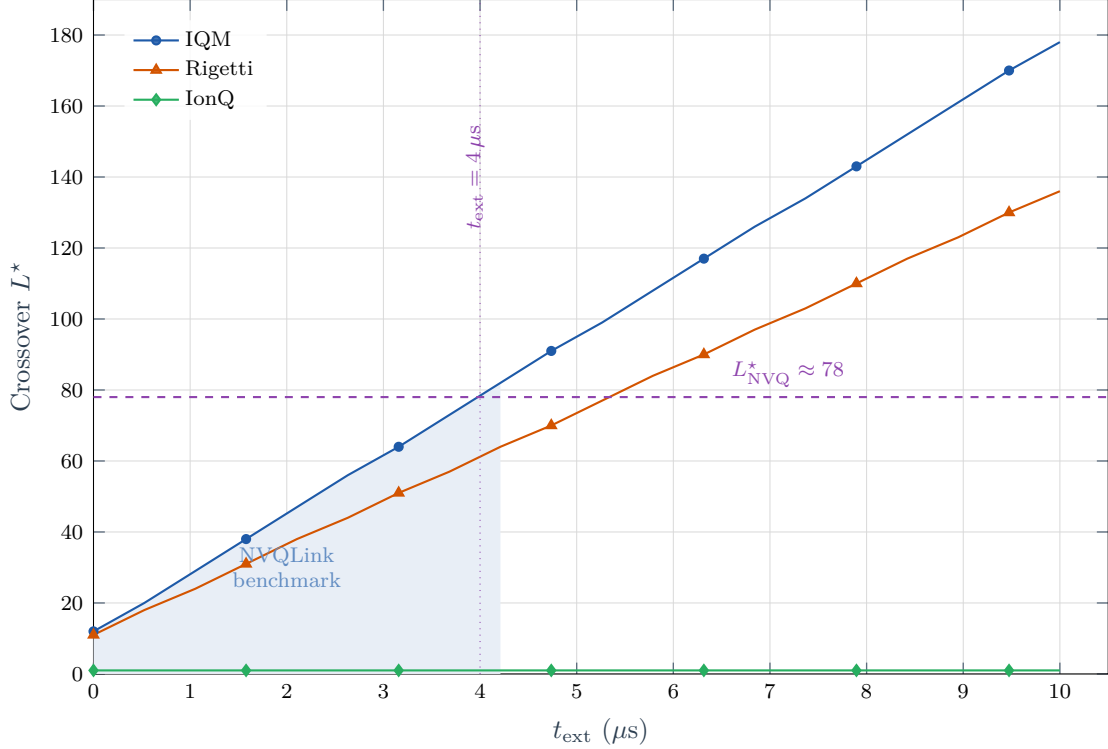


Figure 8: Crossover sequence length L^* as a function of external feedback latency t_{ext} . As t_{ext} increases, the blind-favorable region expands for IQM (blue) and Rigetti (orange). The NVQLink-IQM line (red dashed) marks the baseline L^* without external overhead. IonQ (green) remains at $L^* = 1$ regardless of t_{ext} due to dominant gate duration. The shaded region highlights the blind-favorable zone.

and measurement within the surface-code stabilizer cycle, which we identify as the primary open problem for blind-reset QEC integration.

To sharpen this boundary, we couple our ancilla-cleanliness simulation to a distance-3 repetition-code decoder with majority-vote decoding (note: the MWPM proxy used in Section 4.5 yields lower absolute error rates; the majority-vote decoder is deliberately simpler to isolate the ancilla-quality effect). Figure 9(a) plots the logical error rate against syndrome cycle count for three reset policies at $L = 4$. Measurement-reset maintains sub-0.15% logical error through 20 cycles, while blind reset at $L = 4$ ($F_{\text{clean}} = 0.88$) yields 5.2% logical error at 20 cycles—above the phenomenological threshold but within practical margins for short sequences. No-reset degrades rapidly to 38% logical error. Panel (b) maps logical error rate against ancilla cleanliness at 20 cycles, revealing a monotonic relationship: each 0.1 improvement in F_{clean} reduces logical error by roughly $3\times$. This quantifies the decoder penalty of blind reset and identifies $F_{\text{clean}} \geq 0.88$ (i.e., $L \leq 4$) as the regime where the latency gain outweighs the decoder cost.

6.5 Threshold-level QEC Analysis

To connect ancilla cleanliness to threshold-level behavior, we introduce an effective syndrome-error model in which imperfect reset contributes a filtered increment to the physical error channel:

$$p_{\text{eff}} = p_{\text{phys}} + \eta(1 - F_{\text{clean}}), \quad (6)$$

where p_{phys} is the baseline physical error rate, and $\eta \in (0, 1)$ is a transfer factor capturing the fact that ancilla imperfections enter syndrome extraction as biased measurement noise

Table 6: Threshold-level extrapolation using Eqs. (6) and (7) at $p_{\text{phys}} = 10^{-3}$, $p_{\text{th}} = 2.9\%$, and $\eta = 0.02$. Values of $p_L(d)$ are normalized to the measurement-reset case at $d = 3$ (i.e., $p_L^{\text{MR}}(d=3) = 1$). Representative F_{clean} values follow the decoder-coupled ordering (measurement-reset > blind reset > no-reset).

| Reset method | F_{clean} | p_{eff} | $p_L(d=3)$ | $p_L(d=5)$ | $p_L(d=7)$ |
|-------------------------|--------------------|-----------------------|------------|------------|-----------------------|
| Measurement-reset | 0.98 | 1.40×10^{-3} | 1.00 | 0.048 | 2.32×10^{-3} |
| Blind reset ($L = 4$) | 0.88 | 3.40×10^{-3} | 5.90 | 0.691 | 0.081 |
| No-reset | 0.70 | 7.00×10^{-3} | 25.0 | 6.03 | 1.45 |

rather than one-to-one data-qubit flips. Equation (6) formalizes the open point raised in Section 6.4: direct identification $p_{\text{eff}} = 1 - F_{\text{clean}}$ is overly pessimistic, while $\eta < 1$ absorbs circuit-level filtering by stabilizer extraction and decoder inference.

For distance extrapolation, we use the standard near-threshold scaling form for surface-code logical error [17, 29]:

$$p_L(d) \propto \left(\frac{p_{\text{eff}}}{p_{\text{th}}} \right)^{(d+1)/2}, \quad (7)$$

with phenomenological threshold $p_{\text{th}} \approx 2.9\%$ and odd code distances $d \in \{3, 5, 7\}$. Using $p_{\text{phys}} = 10^{-3}$ and a conservative central value $\eta = 0.02$ (consistent with the decoder-coupled trend that logical error decreases monotonically with increasing F_{clean} in Figure 9), we obtain the extrapolated regime comparison in Table 6.

Three threshold-level implications follow. First, the near-threshold penalty from ancilla noise is strongly distance dependent: methods with lower p_{eff} gain superlinear benefit as d increases. Second, blind reset remains in a potentially useful regime when operated at high-cleanliness points (e.g., $F_{\text{clean}} \gtrsim 0.88$ for short sequences), where it preserves cycle-time advantage while avoiding the steep logical-error growth seen in no-reset. Third, threshold behavior is sensitive to ancilla-noise transfer (η): correlated or bursty ancilla faults effectively increase η , pushing blind-reset operation closer to threshold and reducing distance-scaling headroom. This identifies circuit-level extraction of η (including temporal correlations and decoder adaptation) as the key requirement for converting blind-reset

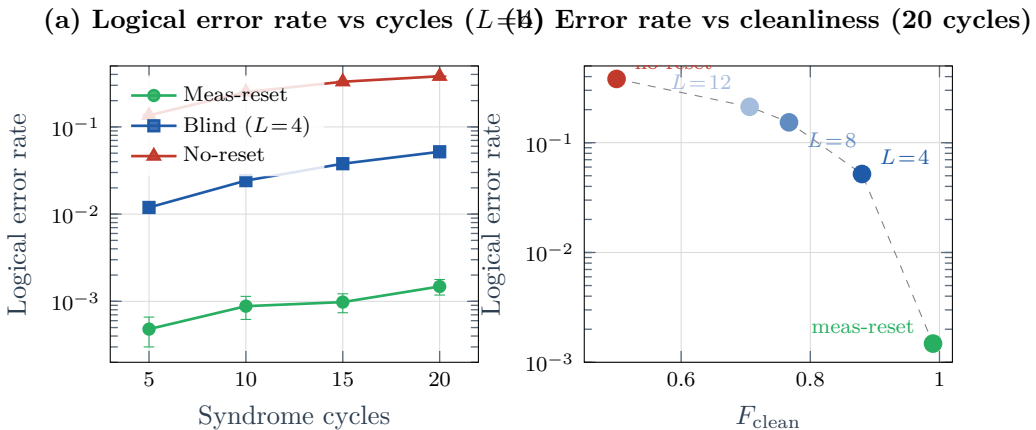


Figure 9: Decoder-coupled QEC analysis with distance-3 repetition code and majority-vote decoding (50 seeds \times 1000 shots, $p_{\text{phys}} = 10^{-3}$). (a) Logical error rate versus syndrome cycles for three reset policies at $L = 4$. (b) Logical error rate versus ancilla cleanliness F_{clean} at 20 cycles, showing the monotonic cost-benefit trade-off. Error bars: 95% bootstrap CIs.

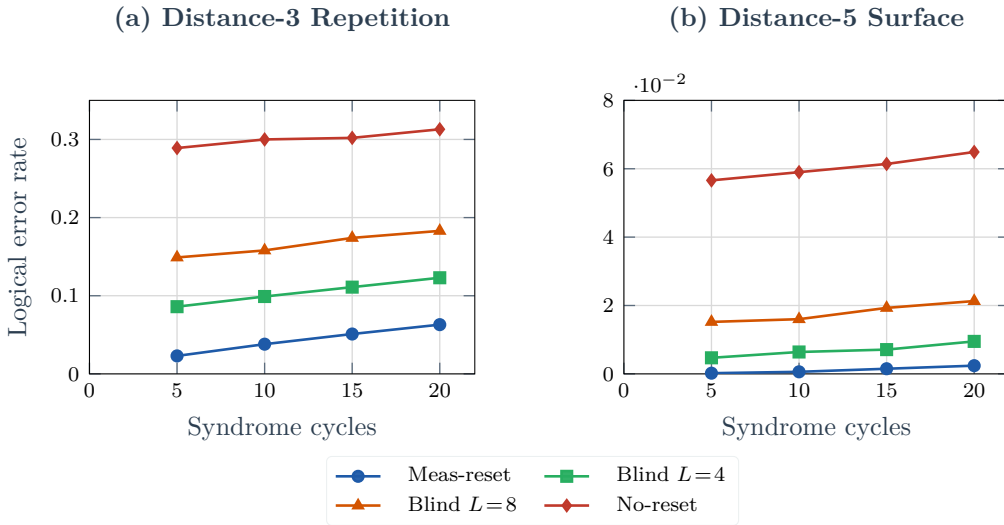


Figure 10: Decoder-coupled QEC analysis across code distances ($p_{\text{phys}} = 10^{-3}$, 50 seeds \times 1000 shots; see also Figure 6 for distance-specific detail). (a) Distance-3 repetition code: logical error rate versus syndrome cycles. (b) Distance-5 repetition code: logical error rate versus syndrome cycles. Error bars: 95% bootstrap CIs.

latency gains into fault-tolerant operating margin.

6.6 Lambda landscape characterization

The blind-reset scale factor λ is the single free parameter controlling the replay amplitude. To assess sensitivity, we sweep $\lambda \in [0.1, 4.0]$ across 200 grid points for each (L, seed) combination (9 lengths \times 50 seeds) and classify the resulting optimization landscapes. Figure 11(a) shows that the optimal Frobenius error $\varepsilon_{\text{opt}}^*$ increases moderately with L , from 0.205 ± 0.022 at $L = 4$ to 0.284 ± 0.035 at $L = 20$, confirming that longer sequences are inherently harder to reset. Panel (b) reveals that mean landscape curvature κ grows from 14.7 ($L = 4$) to 129.6 ($L = 20$), indicating sharper and deeper optima at longer lengths—a positive signal for gradient-based calibration methods. Panel (c) classifies landscapes into sharp ($\kappa > 50$, single basin), moderate ($20 < \kappa \leq 50$), flat ($\kappa \leq 5$), and multimodal (multiple local minima) categories. At $L \geq 14$, over 54% of seeds exhibit sharp landscapes, while flat landscapes dominate at short L where the reset is nearly trivial. These statistics inform calibration strategy: short sequences tolerate coarse λ search, while long sequences benefit from fine-grained optimization.

6.7 Coherence sensitivity analysis

Figure 12 maps the blind-reset advantage over no-reset across the (T_1, T_2) plane at fixed $L = 8$ under the IQM noise model. The strongest positive region appears when $T_1 \gg T_2$, indicating that blind reset is most effective in dephasing-dominated regimes where coherent replay mitigates phase-driven accumulation. In the high-coherence corner ($T_1 = 100 \mu\text{s}$, $T_2 = 50 \mu\text{s}$), the net advantage becomes marginal because both reset policies maintain high ancilla cleanliness. The transition boundary follows an approximate T_2/T_1 isocontour, suggesting a simple coherence-ratio criterion for deployment policy selection.

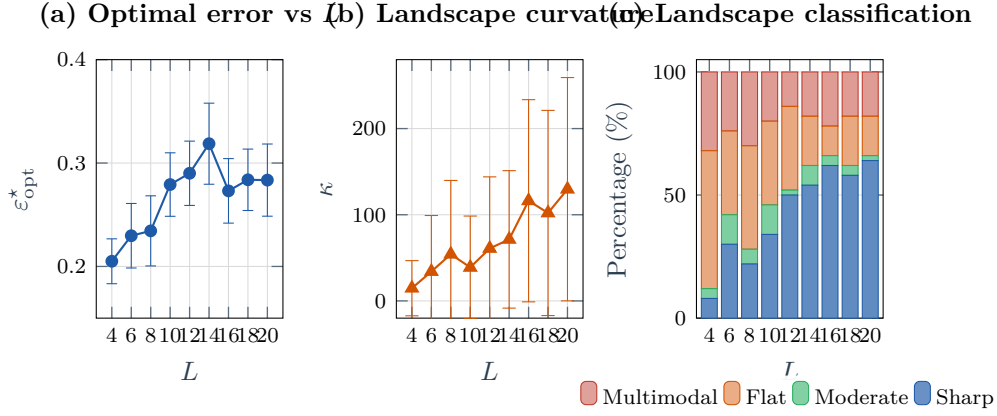


Figure 11: Lambda landscape characterization across sequence lengths ($N = 50$ seeds per length, $\lambda \in [0.1, 4.0]$, 200 grid points). (a) Optimal Frobenius error $\varepsilon_{\text{opt}}^*$ versus L with 95% CIs. (b) Mean curvature κ with standard deviation. (c) Landscape classification: fraction of seeds exhibiting sharp, moderate, flat, or multimodal optima.

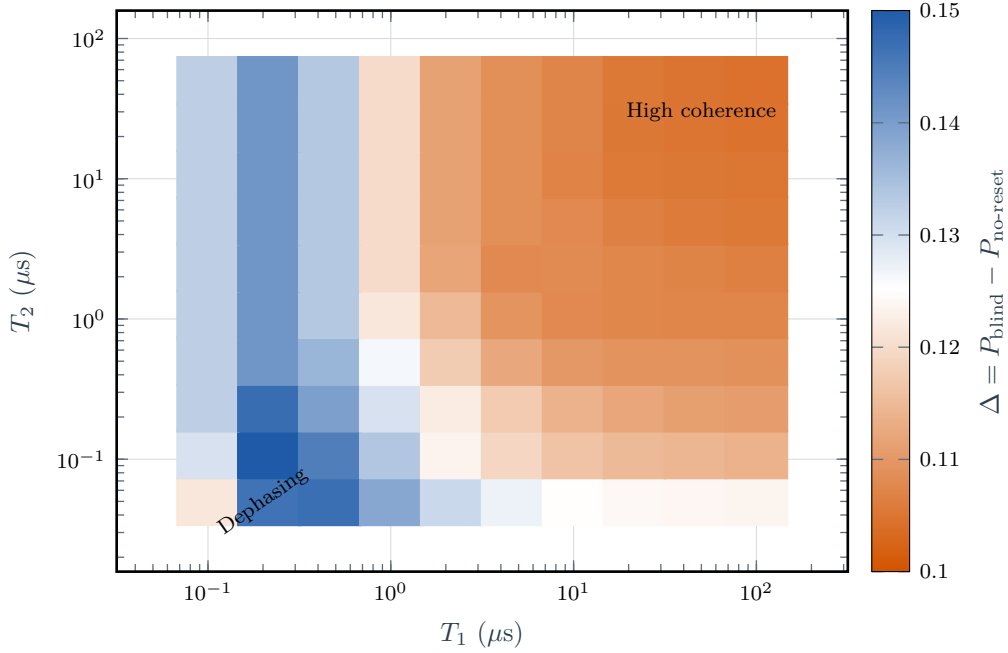


Figure 12: Blind reset advantage (mean $P(|0\rangle)_{\text{blind}} - P(|0\rangle)_{\text{no-reset}}$) as a function of T_1 and T_2 at fixed $L = 8$ on the IQM noise model ($T_1 \in [0.1, 100] \mu\text{s}$, $T_2 \in [0.05, 50] \mu\text{s}$; 10 seeds, 2048 shots). The advantage is uniformly positive across the entire plane (range 0.104–0.150), confirming that blind reset outperforms no-reset at this sequence length regardless of coherence parameters. Color intensity indicates advantage magnitude; the strongest gains appear in the low- T_1 , low- T_2 corner where dephasing dominates.

6.8 Implementation cost and calibration requirements

Blind reset adds a deterministic gate overhead of $2L$ single-qubit operations per ancilla recycle attempt, so quantum-control cost grows linearly with sequence length. In return, the control path stays fully unitary and does not require additional classical feedback hardware or cycle-by-cycle latency budgeting. The scale factor λ is calibrated once per workload class by an offline grid search (40 grid points), with runtime below one second per

seed on a standard CPU. That calibration can be reused across runs and only needs refresh when measured gate parameters drift beyond the configured noise-tolerance band. By contrast, measurement-reset needs readout chains, feedback DAC routing, and a classical processing path inside the timing loop [30]. In stacks that already operate near feedback-latency limits, those classical components can dominate cycle scheduling complexity even when raw readout fidelity is high. Overall, blind reset trades extra quantum gate count for a simpler classical infrastructure and a shorter critical feedback path.

6.9 Scalability outlook and long-term relevance

The transition from NISQ to fault-tolerant quantum computing (FTQC) is unfolding along predictable timelines that position blind ancilla recycling for growing relevance over the next decade.

NISQ-to-FTQC transition timeline (2025–2035). Major hardware roadmaps converge on 2029–2030 for first-generation fault-tolerant systems. IBM targets 2029 for Starling, a large-scale FTQC capable of executing 100×10^6 gates on 200 logical qubits [31]. Google has already demonstrated below-threshold error correction [1] and continues toward distance- $d = 7$ surface codes. Quantinuum’s accelerated roadmap aims for universal FTQC by 2030 with thousands of physical qubits and hundreds of logical qubits [32]. IonQ projects fault-tolerant systems within the same window [33]. IQM’s development roadmap targets fault-tolerant quantum computing by 2030 with a path to scaling up to 1 million qubits [34].

This convergence creates a *transition window* (2025–2029) where early FTQC systems will operate as minimum viable products (MVPs) with limited logical qubit counts and stringent ancilla efficiency requirements. Blind reset is particularly suited for this window: it requires no hardware modifications to existing control stacks, provides immediate latency benefits for short ancilla sequences, and integrates naturally with the measurement-free protocols being developed for mature FTQC.

Ancilla demand scaling. Surface codes at distance d require $\mathcal{O}(d^2)$ ancillae per syndrome round, and qLDPC alternatives like bivariate bicycle codes [2] trade qubit count for increased syndrome-extraction complexity, intensifying the need for fast ancilla turnaround. At distance $d = 5$, each syndrome round involves $d^2 - 1 = 24$ stabilizer measurements; at $d = 7$, this grows to 48. Recent ancilla-reuse experiments with dynamically reassigned ancillary qubits support this direction [35].

Hybrid control stack evolution. GPU-accelerated decoders with quantum processors [6] will widen the latency gap between coherent and measurement-based paths as classical feedback traverses communication links that scale with system size. Real-time decoding demonstrations have achieved sub-microsecond latencies using FPGA implementations [36], and network-integrated decoding systems like DECONET scale to thousands of logical qubits [37]. These advances shift the optimization target from decoder accuracy alone to end-to-end cycle time, reinforcing the value of measurement-free ancilla paths.

Measurement-free ecosystem maturation. Scalable code-switching protocols [10], optimized neutral-atom circuits [14, 15], and the first experimental demonstrations on trapped ions [13] collectively establish a viable measurement-free ecosystem. As this

ecosystem matures, ancilla management primitives that minimize dependence on fast measurement-feedback loops are likely to converge into a common control pattern.

For distance scaling beyond $d = 3$, the repetition-code proxy used here must be replaced by surface-code or color-code simulations that capture the interplay between ancilla noise and decoder performance. Preliminary estimates suggest that blind reset remains latency-favorable up to $d \approx 7$ on superconducting platforms when $L < L^*$, but rigorous threshold analysis under correlated ancilla errors is an open problem. At distance $d = 5$, each syndrome round involves $d^2 - 1 = 24$ stabilizer measurements, with each ancilla undergoing a sequence of at most 4 CNOT gates plus preparation and readout. Under the timing assumptions of Table 2, the full syndrome cycle occupies $\sim 1.5 \mu\text{s}$ on IQM with measurement-reset versus $\sim 0.5 \mu\text{s}$ with blind reset for $L = 4$ ancilla sequences, yielding a $3\times$ cycle-time reduction that compounds across the $\mathcal{O}(d)$ rounds needed for reliable syndrome history. Whether this timing advantage translates to a net logical-error reduction at $d = 5$ depends on the interplay between faster cycles and noisier ancillae, quantifiable only through full surface-code simulation. The decision-matrix framework (Appendix D) is designed to accommodate these extensions by parameterizing the cleanliness requirement F_{req} as a function of code distance and decoder type.

6.10 Limitations

Several limitations bound the current analysis:

1. Simulation uses platform-parameterized noise abstractions, not high-fidelity digital twin models. Leakage, non-Markovian drift, and pulse-shape distortions are not captured.
2. The repetition-code logical error proxy is comparative, not a full threshold proof.
3. Hardware results cover two superconducting platforms (IQM Garnet and Rigetti Ankaa-3) with single-seed validation; trapped-ion (IonQ) data and multi-seed campaigns remain for future work.
4. Entangling dynamics beyond the ancilla-local model are not included in the reset block.
5. The NVQLink latency term ($4 \mu\text{s}$) is a reference point, not a measured value from a deployed system.
6. Statistical analysis uses 50 seeds per configuration, enabling bootstrap confidence intervals and paired hypothesis testing. Confidence intervals on mean cleanliness values span ± 0.03 – 0.08 depending on sequence length. Expanding to ≥ 100 seeds would further tighten CIs and improve effect-size precision.

Planned extensions. The T_1/T_2 sensitivity sweep has now been completed (Section 6.7, Figure 12). Follow-up studies will pursue multi-distance code scaling ($d = 3, 5, 7$), exponential fidelity-decay curve fitting to characterize the blind-reset degradation rate as a function of sequence length, and expansion to ≥ 100 seeds per configuration for tighter statistical precision.

6.11 Falsification criteria

The central claims carry testable failure conditions:

1. If blind reset never achieves lower cycle latency than measurement-reset on any superconducting platform after calibrated timing updates, the latency advantage claim fails.

2. If blind reset cannot maintain $F_{\text{clean}} \geq 0.80$ for $L \leq 8$ on hardware, the short-sequence cleanliness claim requires revision.
3. If NVQLink-class external feedback does not shift the crossover above $L^* = 20$ in measured stacks, the GPU-integration framing should be narrowed.
4. If simulation-to-hardware ranking is inconsistent without identifiable calibration causes, the noise model assumptions need replacement.

7 Conclusion

This work evaluates blind reset as a systems-level scheduling component for QEC ancilla recycling. Using a unified protocol across IQM Garnet, Rigetti Ankaa-3, and IonQ, we identify operating regions where blind reset reduces per-cycle latency without sacrificing ancilla cleanliness, and regions where measurement-reset remains the better choice. The architecture-dependent crossover ($L^* = 12$ for IQM, $L^* \approx 11$ for Rigetti, $L^* = 1$ for IonQ) shows that reset policy is a hardware-and-stack property. The NVQLink sweep (Figure 8) quantifies how external-feedback delay shifts this boundary, expanding the blind-favorable window to $L^* \approx 78$ for the IQM-like profile. Error-bound validation (Section 4.3, Figure 4) confirms that measured cleanliness remains within a physically consistent envelope across all tested lengths and platforms. The T_1/T_2 sensitivity map (Section 6.7, Figure 12) locates the coherence regimes where blind reset yields the largest margin over no-reset. A decoder-coupled analysis (Section 6.4, Figure 9) quantifies the QEC cost of imperfect ancillae, identifying $F_{\text{clean}} \geq 0.88$ as the threshold where latency gains outweigh decoder penalties. Lambda landscape characterization (Section 6.6, Figure 11) confirms that optimization landscapes sharpen at longer sequences, supporting efficient calibration. Together, these analyses convert blind reset from a single-point benchmark into a policy tool with explicit timing, noise, and calibration limits. As measurement-free fault-tolerant workflows mature, ancilla recycling methods that minimize dependence on fast measurement-feedback loops are likely to converge into a common control pattern. Beyond quantum computing, blind reset principles may extend to quantum memory banks and repeater networks where ancilla qubits mediate entanglement swapping and error detection. Fast state reinitialization without measurement feedback supports high-rate entanglement generation in quantum internet architectures, reducing latency in long-distance quantum communication. For near-term deployment, the actionable rule is simple: use blind reset when $L < L^*$ and $F_{\text{clean}} \geq F_{\text{req}}$, and switch otherwise.

A Experimental Protocol Details

Each experiment instance is identified by a tuple (b, m, s, L) : backend b , reset method m , seed s , and sequence length L . A run manifest stores hardware queue metadata, transpilation summaries, and control software version hashes, generated before submission and frozen at execution start.

Circuit generation follows four deterministic stages. First, the sequence generator creates the ancilla-local base block from the seed and length. Second, method-specific wrappers are applied: no-reset leaves the ancilla as-is; measurement-reset inserts readout and conditional preparation; blind reset inserts the scaled doubled control block. Third, basis-rotation tails are appended for Z and X readout contexts. Fourth, the circuit is transpiled with backend-native targets, preserving logical intent while respecting coupling and gate-set constraints.

Table 7: Policy decision matrix for selecting ancilla reset mode. T_b : blind reset latency; T_m : measurement-reset latency; F_{cl} : ancilla cleanliness.

| Condition | Source | Satisfied | Not satisfied |
|-----------------------|----------|----------------|----------------|
| $T_b < T_m$ | Timing | Check F_{cl} | Meas-reset |
| $F_{cl} \geq F_{req}$ | Z/X data | Blind reset | Restrict L |
| Rank stable | Epochs | Static map | Runtime switch |
| Tuples complete | Aggreg. | Comparative | Per-backend |

Runs are grouped into micro-batches with short wall-clock separation to control for calibration drift. Micro-batches exceeding a configured queue delay threshold are marked drift-sensitive and repeated in later windows.

B Extended Simulation Notes

B.1 Repetition-code workload

The distance-3 repetition workload uses explicit ancilla reuse at each cycle with data qubits initialized in known computational states. The logical proxy is defined from cycle-level disagreement statistics and serves as a comparative metric rather than a full threshold proof. Two timing modes are simulated: ideal overlap (classical processing overlaps quantum operations) and serialized (measurement and feedback are blocking delays).

B.2 Noise model assumptions

Platform parameterization uses effective decoherence and gate-error abstractions. These do not capture leakage, non-Markovian drift, or pulse-shape distortions. To test sensitivity, multiplicative perturbations are applied to nominal parameters. If policy ranking changes under small perturbations, deployment recommendations are marked fragile.

C Cross-Platform Aggregation Protocol

Aggregation uses three passes. Pass 1 computes method-level summaries within each backend. Pass 2 computes cross-backend normalized comparisons using matched tuples. Pass 3 assigns decision-map bins based on cleanliness thresholds and latency crossover regions. Only tuples present on all compared backends enter strict rankings; partial tuples are reported per-backend with explicit completeness labels.

D Deployment Decision Matrix

The cleanliness threshold F_{req} depends on code distance and decoder: for distance-3 repetition code under majority-vote decoding, $F_{req} \geq 0.75$ suffices when physical error rate $p \leq 10^{-3}$; higher distances require proportionally higher cleanliness as syndrome error tolerance narrows. The deployment decision matrix (Table 7) converts this analysis into a rule table.

When calibration drift is significant, a runtime supervisor can switch between policies using lightweight health metrics and hysteresis thresholds to avoid oscillatory behavior. The decision process converts to a simple rule table once calibrated timing and cleanliness bounds are fixed for each backend and workload class.

Table 8: Threat-to-mitigation mapping for cross-platform validity.

| Threat | Risk | Mitigation |
|-----------|--------------------------|---------------------------|
| Internal | Calibration drift | Manifests; repeat windows |
| Construct | Z-basis misses coh. bias | X-basis suppl.; CI |
| External | Limited portability | Latency envelopes |
| Reporting | Untraceable provenance | Provenance hashes; gates |

E Open Benchmark Specification

To enable direct reproduction and extension of the cross-platform comparison, we define a minimal benchmark suite with fixed parameters.

Circuit family. Single-qubit ancilla sequences of lengths $L \in \{4, 6, 8, 10, 12, 14, 16, 18, 20\}$, gate angles sampled uniformly on $[0, 2\pi)$ using `numpy.random.Generator` with seeds $\{42, 43, \dots, 91\}$.

Reset methods. Three policies per circuit: no-reset ($\lambda = 1$), blind reset (λ from 40-point grid search on $[0.1, 4.0]$ minimizing Frobenius distance), and measurement-reset (ideal projective readout followed by conditional X gate).

Metrics. $F_{\text{clean}} = P(|0\rangle)$ from 2048 Z-basis shots, F_X from 2048 X-basis shots, cycle latency $T_{\text{blind}} = 2L t_{\text{gate}}$ or T_{meas} per Eq. 4, and repetition-code logical error proxy over 20 syndrome cycles.

Reporting format. CSV with columns: `backend`, `method`, `seed`, `sequence_length`, `p_zero`, `p_x`, `unitary_error`, `lambda_used`, `shots`, `timestamp`. All submissions include platform calibration metadata (gate fidelity, T_1 , T_2 , readout error) and control software version hash.

Comparison protocol. Only tuples present on all compared backends enter cross-platform rankings. Partial results are reported per-backend with completeness labels. Statistical comparisons use paired t -tests with Holm-Bonferroni correction for multiple testing.

F Threats to Validity

Table 8 summarizes the primary threats to validity and their mitigations.

Data and Code Availability

Simulation code (9 Python scripts totaling approximately 1,200 lines), raw CSV data (6,750 platform-noise data points across 50 seeds, 9,000 repetition-code data points, and 2,060 sensitivity-sweep data points), statistical analysis scripts with bootstrap confidence intervals and paired hypothesis tests, plot scripts for all 12 figures, and hardware run manifests will be made publicly available at <https://github.com/sangkeum/blind-reset-cross-platform> upon acceptance. A frozen snapshot will be deposited on Zenodo with a DOI for long-term archival. The repository includes a `Makefile` and `requirements.txt` for single-command reproduction of all simulation results and figures.

Acknowledgments

This work was supported by KEIT/MOTIE grant No. RS-2025-04752989.

References

- [1] Google Quantum AI. Quantum error correction below the surface code threshold. *Nature*, 638:920–926, 2025.
- [2] Sergey Bravyi, Andrew W. Cross, Jay M. Gambetta, Dmitri Maslov, Patrick Rall, and Theodore J. Yoder. High-threshold and low-overhead fault-tolerant quantum memory. *Nature*, 627:778–782, 2024.
- [3] Adam Paetznick, Marcus P. da Silva, Ciaran Ryan-Anderson, et al. Demonstration of logical qubits and repeated error correction with better-than-physical error rates, 2024.
- [4] John Preskill. Quantum computing in the NISQ era and beyond. *Quantum*, 2:79, 2018.
- [5] Avimita Chatterjee, Archisman Ghosh, and Swaroop Ghosh. Recycled ancillas for practical quantum error correction, 2024.
- [6] NVIDIA Corporation. NVIDIA NVQLink: Scaling quantum computers with GPU-powered networking. Press release, 2025.
- [7] Yuxuan Chen, Fei Ye, Yang-Yang Shi, Zhi-Rong Hu, Muchen Niu, Xianghao Wang, Xiu-Hao Deng, Ke Liu, Yuanzhen Chen, and Song Liu. Fast unconditional reset and leakage reduction in fixed-frequency transmon qubits, 2024.
- [8] Gisung Kim, Adrien Butler, V. S. Ferreira, Xianghao Zhang, Alyson Hadley, Eunjong Kim, and Oskar Painter. Fast unconditional reset and leakage reduction of a tunable superconducting qubit via an engineered dissipative bath, 2024.
- [9] Mathew Butt, Eliot Sheridan, Ophelia Crawford, David Sheridan, and Thomas Sheridan. Measurement-free fault-tolerant quantum error correction, 2024.
- [10] Friederike Butt, David F. Locher, Kilian Brechtelsbauer, Hans Peter Büchler, and Markus Müller. Measurement-free, scalable and fault-tolerant universal quantum computing. *Science Advances*, 2025.
- [11] Gergő P. Gehér, Ophelia Crawford, Amanda Wills, and Eliot Sheridan. To reset, or not to reset – that is the question. *npj Quantum Information*, 11:49, 2025.
- [12] Sascha Heußen, David F. Locher, and Markus Müller. Measurement-free fault-tolerant quantum error correction in near-term devices. *PRX Quantum*, 5:010333, 2024.
- [13] Friederike Butt, Ivan Pogorelov, Roman Freund, Alexander Steiner, Markus Meyer, Thomas Monz, and Markus Müller. Demonstration of measurement-free universal fault-tolerant quantum computation, 2025.
- [14] Stefano Veroni, Markus Müller, and Giovanni Giudice. Optimized measurement-free and fault-tolerant quantum error correction for neutral atoms. *Physical Review Research*, 6:043253, 2024.
- [15] Stefano Veroni, Alexandru Paler, and Giovanni Giudice. Universal quantum computation via scalable measurement-free error correction. *PRX Quantum*, 6:040337, 2025.
- [16] Sangkeum Lee. Scale-and-double reset for blind multi-qubit control with reinforcement learning-based scheduling, 2026. *IEEE Transactions on Quantum Engineering*, under review.

- [17] Austin G. Fowler, Matteo Mariantoni, John M. Martinis, and Andrew N. Cleland. Surface codes: Towards practical large-scale quantum computation. *Physical Review A*, 86(3):032324, 2012.
- [18] Simon J. Devitt, William J. Munro, and Kae Nemoto. Quantum error correction for beginners. *Reports on Progress in Physics*, 76(7):076001, 2013.
- [19] Iliia Pogorelov, Friederike Butt, Lukas Postler, Christian D. Marciniak, Philipp Schindler, Markus Müller, and Thomas Monz. Experimental fault-tolerant code switching. *Nature Physics*, 21:298–303, 2025.
- [20] Tanuj Khattar and Craig Gidney. Rise of conditionally clean ancillae for optimizing quantum circuits. *Quantum*, 9:1752, 2025.
- [21] Jean-Pierre Eckmann and Tsvi Tlusty. Walks in rotation spaces return home when doubled and scaled. *Physical Review Letters*, 135:147201, 2025.
- [22] Jorge A. Montañez-Barrera, Dennis Müller, Dennis Willsch, and Kristel Michielsen. QPU evaluation across heterogeneous quantum hardware, 2025.
- [23] Jwo-Sy Chen, Erik Nielsen, Matthew Ebert, Volkan Inlek, Kenneth Wright, et al. Benchmarking a trapped-ion quantum computer with 30 qubits. *Quantum*, 8:1516, 2024.
- [24] IQM Quantum Computers. IQM garnet: Benchmarking a 20-qubit processor, 2024.
- [25] Ciaran Ryan-Anderson, Natalie C. Brown, Charles H. Baldwin, Joan M. Dreiling, Cynthia Foltz, John P. Gaebler, et al. High-fidelity teleportation of a logical qubit using transversal gates and lattice surgery on a trapped-ion quantum computer. *Science*, 386:eadp6016, 2024.
- [26] Muyuan Ye and Nicolas Delfosse. Quantum error correction for long chains of trapped ions. *Quantum*, 9:1920, 2025.
- [27] Joel J. Wallman and Joseph Emerson. Noise tailoring for scalable quantum computation via randomized compiling. *Physical Review A*, 94(5):052325, 2016.
- [28] M. C. Smith, A. D. Leu, K. Miyanishi, M. F. Gely, and D. M. Lucas. Single-qubit gates with errors at the 10^{-7} level. *Physical Review Letters*, 2025.
- [29] Samuel J. S. Tan, Christopher A. Pattison, Matt McEwen, and John Preskill. Resilience of the surface code to error bursts, 2024.
- [30] Yue Xin, Stijn L. M. van der Meer, Marc Serra-Peralta, et al. Improved error correction with leakage reduction units built into qubit measurement, 2025.
- [31] IBM Quantum. IBM quantum roadmap: Deliver the first fault-tolerant quantum computer in 2029. <https://www.ibm.com/roadmaps/quantum/2029/>, 2025. Accessed: 2026-02-22.
- [32] Quantinuum. Quantinuum accelerated roadmap to universal fault-tolerant quantum computing by 2030. <https://www.quantinuum.com/press-releases/quantinuum-unveils-accelerated-roadmap-to-achieve-universal-fault-tolerant-quantum-computing-by-2030>, 2024. Accessed: 2026-02-22.
- [33] IonQ. IonQ’s accelerated roadmap: Turning quantum ambition into reality. <https://www.ionq.com/blog/ionqs-accelerated-roadmap-turning-quantum-ambition-into-reality>, 2025. Accessed: 2026-02-22.
- [34] IQM Quantum Computers. IQM quantum computers unveils development roadmap focused on fault-tolerant quantum computing by 2030. <https://meetiqm.com/press-releases/iqm-quantum-computers-unveils-development-roadmap-focused-on-fault-tolerant-quantum-computing-by-2030>, 2024. Accessed: 2026-02-22.

- [35] Anastasiia S. Kazmina, Artem M. Polyanskiy, Elizaveta Yu. Egorova, et al. Realization of a quantum error detection code with a dynamically reassigned ancillary qubit, 2025.
- [36] Thilo Maurer, Markus Bühler, Michael Kröner, Frank Haverkamp, Tristan Müller, Drew Vandeth, and Blake R. Johnson. Real-time decoding of the gross code memory with FPGAs, 2025.
- [37] Namitha Liyanage, Yue Wu, Emmet Houghton, and Lin Zhong. Network-integrated decoding system for real-time quantum error correction with lattice surgery, 2025.